THE JOURNAL OF NAVIGATION (2019), **72**, 1378–1398.
doi:10.1017/S0373463319000353

Improved Integral LOS Guidance and Path-Following Control for an Unmanned Robot Sailboat via the Robust Neural Damping Technique

Guoqing Zhang[1,2], Jiqiang Li[1], Bo Li[1] and Xianku Zhang[1]

[1](*Navigation College, Dalian Maritime University, Dalian, China*)
[2](*Collaborative Innovation Center for Transport Studies, Dalian Maritime University, Dalian, China*)
(E-mail: zhangxk@dlmu.edu.cn)

This paper introduces a scheme for waypoint-based path-following control for an Unmanned Robot Sailboat (URS) in the presence of actuator gain uncertainty and unknown environment disturbances. The proposed scheme has two components: intelligent guidance and an adaptive neural controller. Considering upwind and downwind navigation, an improved version of the integral Line-Of-Sight (LOS) guidance principle is developed to generate the appropriate heading reference for a URS. Associated with the integral LOS guidance law, a robust adaptive algorithm is proposed for a URS using Radial Basic Function Neural Networks (RBF-NNs) and a robust neural damping technique. In order to achieve a robust neural damping technique, one single adaptive parameter must be updated online to stabilise the effect of the gain uncertainty and the external disturbance. To ensure Semi-Global Uniform Ultimate Bounded (SGUUB) stability, the Lyapunov theory has been employed. Two simulated experiments have been conducted to illustrate that the control effects can achieve a satisfactory performance.

KEYWORDS

1. Path-following. 2. URS. 3. Integral LOS guidance. 4. Robust neural damping technique.

Submitted: 26 November 2018. Accepted: 16 April 2019. First published online: 5 July 2019.

1. INTRODUCTION. Sail is one of the most ancient forms of marine surface vehicle propulsion, using the forces of the wind to propel a vessel (Carter and Carter, 2010; Perez, 2005). In recent years, Unmanned Robot Sailboats (URS) have been developed for use in fields such as ocean investigation and exploitation due to their low energy use. A sailboat requires renewable energy instead of fossil fuels and can undertake long duration tasks (Viel et al., 2018; Alves and Cruz, 2014). However, the cumbersome operation of sails

could produce difficulties in the stabilisation of a closed-loop control system (Illingworth, 1997). Although strong winds could supply enough power for the sailboat, it may also cause system instability, even leading to the invalidation of existing control schemes (Zhang et al., 2015). Thus, an intelligent guidance and control method for a URS merits further investigation.

Recently, there has been a significant interest in the control of URS. A variety of theoretical research has been reported: for example, short course racing control (Stelzer and Proll, 2008; Tagliaferri and Viola, 2017) and the reactive path planning approach (Plumet et al., 2015). In Yeh and Bin (1992), the fuzzy relationship between the sail angle and the apparent wind direction was formulated and a fuzzy control algorithm was applied to achieve the course control of a sailboat. Furthermore, considering different weather cases, especially upwind or downwind legs, Abril et al. (1997) discussed the dynamic characteristics of sailboats including the aerodynamic and hydrodynamic forces. Their proposed control algorithm could maintain the highest possible speed and follow the reference heading with a desirable response. Since the roll dynamics of sailboats have a crucial role for evaluation of the control strategies, a nonlinear four degrees of freedom mathematical model was presented in Xiao et al. (2011), Wille et al. (2016) and Deng et al. (2018), based on previous work. Xiao and Jouffroy (2014) used a conventional rudder and a simple moving mass system as the controllable variables to derive a backstepping-based course-keeping control law for a keeled sailboat (considering the rolling motion) and a Globally Uniform Asymptotic Stability (GUAS) was obtained for the closed-loop system.

In the aforementioned literatures, the actuators' gain function is assumed to be known for the control design. That does not meet engineering practice and may limit the application of these theoretical results. Course-keeping control is selected as the automatic task of interest, which is not sufficient for implementing the autonomous navigation of a URS (Tagliaferri et al., 2014; Guo et al., 2011). In the authors' previous work (Zhang et al., 2017; Qiao and Zhang, 2018), the underactuated surface vessel was considered as the test vessel and the constraint of the actuators' gain uncertainty was released by utilising Dynamic Surface Control (DSC) and the robust neural damping technique. To further improve the implementability of the theoretical algorithm, a new reactive navigation approach, based on artificial potential fields, was developed to tackle uncontrollable and changeable environment perturbations (Petres et al., 2012), that is, the stochastic obstacles that exist in the vicinity of the reference route. In the algorithm, a zigzag trajectory is employed to achieve the target navigation of sailboats, and the periodically updated potential could guarantee the real-time computation of a feasible heading. In Corno et al. (2016), the path-following task of the keeled sailboat was addressed by combining a heading controller, acting on the rudder, and a velocity optimiser, acting on the sails. The results of an experiment on an instrumented scale model have validated the near-optimal performance of the proposed scheme. Note that, in nautical practice, the varying nature of wind propulsion is not the sole factor affecting the sail/yacht dynamics. The varying destination, on the waypoint-based planned route, may change the wind conditions for the URS. Therefore, intelligent guidance needs to be designed for the URS, especially for tacking and gybing cases. In other research, (Serrano et al., 2014; Statheros et al., 2008; Li and Tong, 2018a), the Line-Of-Sight (LOS) guidance principle was detailed and incorporated with the stability theory of cascade interconnected systems to achieve a straight-line path-following mission. Further LOS guidance with the integral effect (that is, the integral LOS law) could successfully

https://doi.org/10.1017/S0373463319000353 Published online by Cambridge University Press

counteract the current disturbances, without the risk of wind-up effects (Caharija et al., 2012; Li and Tong, 2018b). However, the integral LOS principle may not be applicable to the practical condition "waypoint-based planned route for the URS". In addition, especially for the upwind and downwind conditions, the control objective should be guaranteed by employing both the rudder and the sail.

Motivated by the above observations, this paper focuses on the intelligent guidance and control design for a URS in a marine environment. For the guidance term, an improved version of the integral LOS principle is developed for waypoint-based path-following control. For the control term, the merit of NNs approximation and the robust neural damping technique are employed, and the constraint of control gain uncertainty is compensated by the gain-related adaptive parameter. Furthermore, the path-following capability of the proposed scheme is demonstrated through theoretical analysis and numerical experiments. The main contributions of this paper can be summarised as follows:

(1) Based on the conventional integral LOS principle, an improved version is developed to implement the waypoint-based path-following control of URS, with a spontaneous selecting strategy depending on the random wind direction and the varying route reference. In addition, for the tacking and gybing scenarios, the safety bandwidth constraint is set for the zigzag trajectory to improve its implementability.
(2) A novel robust adaptive control algorithm is proposed for URS with the sail angle and the rudder angle as the control inputs. In the control law, due to the merit of a Neural Networks (NNs) approximator, information on the model structure, parameters and the environment disturbance is not required, and only one gain-related adaptive parameter is updated online to compensate for the effect of actuator gain uncertainty. In addition, the advantageous damping term in the controller could reduce the rolling motion during the switch operation of the desired route segment or the zigzag trajectory. Thus, the derived control law is superior in terms of concise form and safety, which could facilitate its application in practice.

2. PROBLEM FORMULATION AND PRELIMINARIES.

Throughout this paper, $|\cdot|$ is the absolute operator of a scalar. $\|\cdot\|$ indicates the Euclidean norm of a vector and $\|\cdot\|_F$ describes the Frobenius norm. For a given matrix $\boldsymbol{A} = [a_{i,j}] \in \mathbb{R}^{m\times n}$, $\|\boldsymbol{A}\|_F^2 = \mathrm{tr}\{\boldsymbol{A}^T\boldsymbol{A}\} = \sum_{i=1}^{m}\sum_{j=1}^{n} a_{i,j}^2$ · sgn indicates the sign function.

2.1. *4-DOF dynamic model of URS.*

A class of Four Degrees-Of-Freedom (4-DOF) URS model based on Fossen's methodology (Xiao and Jouffroy, 2014), considering the rolling motion, can be expressed as:

$$\begin{cases} \dot{x} = u\cos(\psi) - v\cos(\phi)\sin(\psi) \\ \dot{y} = u\sin(\psi) + v\cos(\phi)\cos(\psi) \\ \dot{\phi} = p \\ \dot{\psi} = r\cos(\phi) \end{cases} \tag{1}$$

https://doi.org/10.1017/S0373463319000353 Published online by Cambridge University Press

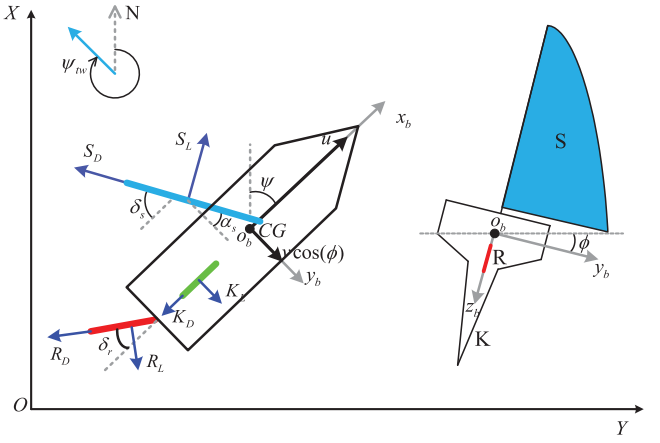

Figure 1. Illustration of the Earth-fixed frame and body-fixed frame.

$$\begin{cases} \dot{u} = \dfrac{1}{m_u}(S_u + R_u + K_u + m_v vr - D_u) + d_{wu} \\ \dot{v} = \dfrac{1}{m_v}(S_v + R_v + K_v + m_u ur - D_v) + d_{wv} \\ \dot{p} = \dfrac{1}{m_p}(S_p + R_p + K_p - g(\phi) - D_p) + d_{wp} \\ \dot{r} = \dfrac{1}{m_r}(S_r + R_r + K_r - (X_{\dot{u}} - Y_{\dot{v}})uv - D_r) + d_{wr} \end{cases} \tag{2}$$

with:

$$g(\phi) = mgGM_t \sin(\phi)\cos(\phi) \tag{3}$$

where $m_u = m - X_{\dot{u}}$, $m_v = m - Y_{\dot{v}}$, $m_p = I_x - K_{\dot{p}}$, $m_r = I_z - N_{\dot{r}}$, m is the mass of the URS and GM_t is the transverse metacentric height. $\boldsymbol{\eta} = [x, y, \phi, \psi]$ (see Figure 1) describes the position, roll angle and yaw angle in the inertial reference frame (n-frame). $\boldsymbol{\nu} = [u, v, p, r]$ describes the surge, sway, roll and yaw velocities in the body fixed frame (b-frame). $d_{wi}, i = u, v, p, r$ describes the environmental disturbance forces or moments. $[S_i, R_i, K_i, D_i]$, $i = u, v, p, r$ describes the forces or moments generated by sail, rudder, keel and hull along the x-axis, y-axis or z-axis in the b-frame.

In a keeled robot sailboat, the keel is mainly used to offset the rolling force or moments caused by the sail, see Figure 1. The apparent wind speed U_{aw} and true wind speed U_{tw} can be transformed from n-frame to b-frame via the sailboat's wind speed (Arredondo-Galeana and Viola, 2018). Then the apparent wind angle psi_{aw} in the b-frame can be described as $\psi_{aw} = \arctan 2(U_{awv}, -U_{awu})$. The attack angle for the sail is expressed by

$$\alpha_s(\cdot) = \psi_{aw}(\cdot) - \delta_s \tag{4}$$

δ_s is the sail angle, which is obtained from a look-up table (Xiao and Jouffroy, 2014).

https://doi.org/10.1017/S0373463319000353 Published online by Cambridge University Press

The lift and drag force, generated by the sail in the apparent wind can be computed as:

$$\begin{cases} S_L = \dfrac{1}{2}\rho_a A_s U_{aw}^2 C_{S_L}(\alpha_s) \\ S_D = \dfrac{1}{2}\rho_a A_s U_{aw}^2 C_{S_D}(\alpha_s) \end{cases} \tag{5}$$

where ρ_a denotes the air density and A_s denotes the area of sail. C_{S_L} and C_{S_D} denote the lift and drag coefficients of the sail. According to Equation (5) and Figure 1, $[S_u, S_v, S_p, S_r]$ can be obtained. In a similar way, the force and moments $[R_i, K_i, D_i]$, $i = u, v, p, r$ generated by rudder, keel and hull can be derived.

The turning moment of the rudder can be described as:

$$R_r = -\frac{1}{2}\rho_w A_r U_{ar}^2(\alpha_R)|x_r| \tag{6}$$

where ρ_w is the water density, A_r is the area of rudder, $C_{R_L}(\alpha_R)$ is the lift coefficient of the rudder and α_R is the attack angle of the rudder, $|x_r|$ is the x coordinate of the rudder's centroid in the b-frame and U_{ar} is the apparent speed of the rudder with $U_{ar}^2 = \sqrt{u^2 + v^2}$.

Remark 1: The 4-DOF nonlinear mathematical model Equations (1) and (2) has been established in Wille et al. (2016) and Xiao and Jouffroy (2014). The sailboat is separated into four parts (that is, the sail, rudder, keel and hull), and the forces and moments acting on the sailboat are the integration of the effects of each part. The sailboat receives several available online datums, such as true wind direction and velocity, which can be collected by anemometers and wind vanes and the heading angle which can be measured by a compass. Hence, the nonlinear mathematical model is reasonable and effective.

A few assumptions applied throughout this paper are:

Assumption 1: There exist unknown positive constants $\bar{d}_{wi}$, satisfied the disturbance terms d_{wi} due to the environment and are bounded, such that $d_{wi} \leq \bar{d}_{wi}$.

Assumption 2: Based on the systematic analysis in Do (2010), the sway motion of under-actuated ships is passive-bounded stable. This means that the sway velocity is bounded as the surge and yaw motions are uniform and ultimately bounded.

Assumption 3: The robot sailboat is hypothesised as rigid and in considering 4-DOFs, the heaving and pitching motions are ignored. The robot sailboat is presumed to sail in still waters, that is, the current is ignored.

2.2. *Modelling of tacking and gybing.* Fully autonomous sailboats still have a huge challenge. It is complicated work to operate the rudder to steer on the desired path and simultaneously adjust the sail to get the best performance.

Being different from propeller-driven ships, the main feature for sailboats is the sail as an actuator in the surge degree of freedom rather than propellers. The sail is greatly influenced by the weather. Therefore, in order to steer the sailboat along the desired route generated by waypoints, not all the legs are navigable, see Figure 2(a). Figure 2 illustrates

https://doi.org/10.1017/S0373463319000353 Published online by Cambridge University Press

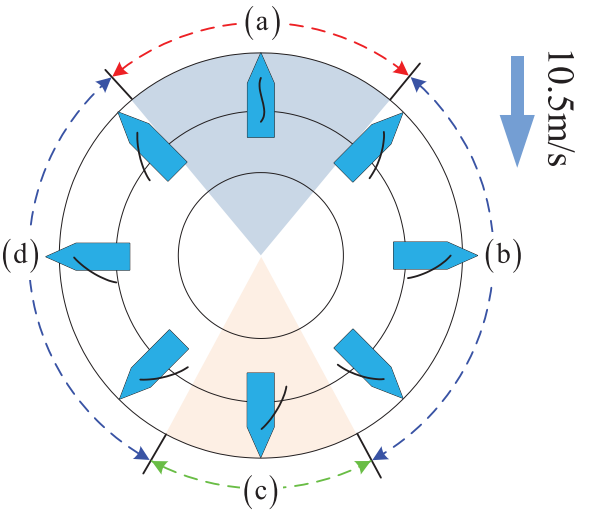

Figure 2. Zones of sail: (a) No-go zone; (b), (d) Navigable zone; (c) Do not-go zone.

the relationship between the sailboat courses and the wind direction. It is can be seen that some courses are navigable (Figures 2(b) and 2(d)), and some courses are ineffective (Figure 2(c)). These restrictions have to be taken into account in planning the route for a sailing trip. Therefore, the route may contain multiple sections, with tacks or gybes between them. To avoid these constraints and reach any target autonomously, a zigzag route must be considered.

The objective contains two points: (1) To develop an improved integral LOS guidance scheme which could provide the reference path guidance law (consists of Navigable zone, No-go zone and Do not-go zone). (2) To develop an adaptive neural control law to stabilise the sailboat to the desired heading angle effectively.

2.3. *RBF-NNs-based function approximation.* In control engineering, Radial Basic Function Neural Networks (RBF-NNs) are generally employed as an effective tool for modelling nonlinear functions due to their fine capabilities in function approximation (Xu and Sun, 2018). In this paper, RBF-NNs are employed in control design to deal with the structure and parameter uncertainties. The robust neural damping technique is further designed to promote the robustness and the stability of the closed-loop system. It is vital for control design, which facilitates the concise form and small computation burden in practical control engineering. To that end, Lemma 1 is helpful for the control design.

Lemma 1 (Li and Tong, 2018a; Xu and Shou, 2018): For any given continuous function $f(x)$ with $f(\mathbf{0}) = 0$, defined on a compact set $\Omega_x \subset \mathscr{R}$, can be approximated by RBF-NNs with random precision. It can be described as:

$$f(\boldsymbol{x}) = \boldsymbol{S}(\boldsymbol{x})\boldsymbol{A}\boldsymbol{x} + \varepsilon(\boldsymbol{x}), \quad \forall \boldsymbol{x} \in \Omega_x \tag{7}$$

where $\boldsymbol{S}(\boldsymbol{x}) = [s_1(\boldsymbol{x}), s_2(\boldsymbol{x}), \ldots, s_l(\boldsymbol{x})]$ is a vector of Gaussian function, expressed in the following elements as Equation (8), $l > 1$ is the NN node number, μ_i and ξ_i denotes the centre

https://doi.org/10.1017/S0373463319000353 Published online by Cambridge University Press

of the receptive field and the width of the Gaussian function, respectively.

$$s_i(\boldsymbol{x}) = \frac{1}{\sqrt{2\pi}\xi_i} \exp\left(-\frac{(x-\mu_i)^{\mathrm{T}}(x-\mu_i)}{2\xi_i^2}\right), \quad i = 1, 2, \ldots, l \tag{8}$$

$\varepsilon(\boldsymbol{x})$ is the approximation error with unknown upper bound $\bar{\varepsilon}$, n is the dimension of x and $\boldsymbol{A}$ is a weight matrix, expressed as Equation (9).

$$\boldsymbol{A} = \begin{bmatrix} w_{11} & w_{12} & \cdots & w_{1n} \\ w_{21} & w_{22} & \cdots & w_{2n} \\ \vdots & \vdots & \ddots & \vdots \\ w_{l1} & w_{l2} & \cdots & w_{ln} \end{bmatrix} \tag{9}$$

3. IMPROVED INTEGRAL LOS GUIDANCE FOR ROBOT SAILBOAT. In this section, the improved integral LOS guidance is analysed in two parts: the navigable path-following guidance (navigable mode) and the complicated manoeuvring guidance (such as upwind mode and downwind mode). Therefore, the improved integral LOS framework is developed for further guidance design. As is described in Figure 3, a parameterised path is generated by waypoints. ω denotes the path variable and the inertial position of the reference path is denoted by $(x_r(\omega), y_r(\omega))$ with arbitrary given ω. The path-tangential angle $\psi_r(\omega)$ is calculated by $\psi_r(\omega) = \mathrm{atan2}(y_r', x_r')$ with $x_r' = \partial x_r/\partial\omega, y_r' = \partial y_r/\partial\omega$. The present position of the robot sailboat is denoted by (x, y), the along-track error x_e and the cross-track error y_e related to the reference path can be derived by Equation (10):

$$\begin{bmatrix} x_e \\ y_e \end{bmatrix} = \begin{bmatrix} \cos(\psi_r) & \sin(\psi_r) \\ -\sin(\psi_r) & \cos(\psi_r) \end{bmatrix} \begin{bmatrix} x - x_r(\omega) \\ y - y_r(\omega) \end{bmatrix} \tag{10}$$

Taking the time derivative of x_e, y_e, we can obtain:

$$\begin{cases} \dot{x}_e = (\dot{x} - \dot{x}_r)\cos(\psi_r) + (\dot{y} - \dot{y}_r)\sin(\psi_r) + \dot{\psi}_r y_e \\ \dot{y}_e = -(\dot{x} - \dot{x}_r)\sin(\psi_r) + (\dot{y} - \dot{y}_r)\cos(\psi_r) + \dot{\psi}_r y_e \end{cases} \tag{11}$$

Substituting Equation (1) into Equation (11), it follows that:

$$\begin{cases} \dot{x}_e = U\cos(\psi - \psi_r + \beta) + \dot{\psi}_r y_e - u_p \\ \dot{y}_e = U\sin(\psi - \psi_r + \beta) + \dot{\psi}_r x_e \end{cases} \tag{12}$$

where $U^2 = \sqrt{u^2 + (v\cos(\phi))^2}$ denotes the resultant speed of the robot sailboat $\beta = \mathrm{atan2}(v\cos\phi, u)$ and denotes the sideslip angle, see Figure 3, and u_p denotes the velocity of the virtual reference point described as:

$$u_p = \dot{\omega}\sqrt{x_r'^2 + y_r'^2} \tag{13}$$

Furthermore, the guidance law is derived as:

$$\psi_{ILOS} = \psi_r - \arctan\left(\frac{y_e + \sigma y_{\mathrm{int}}}{\Delta}\right) - \beta \tag{14}$$

https://doi.org/10.1017/S0373463319000353 Published online by Cambridge University Press

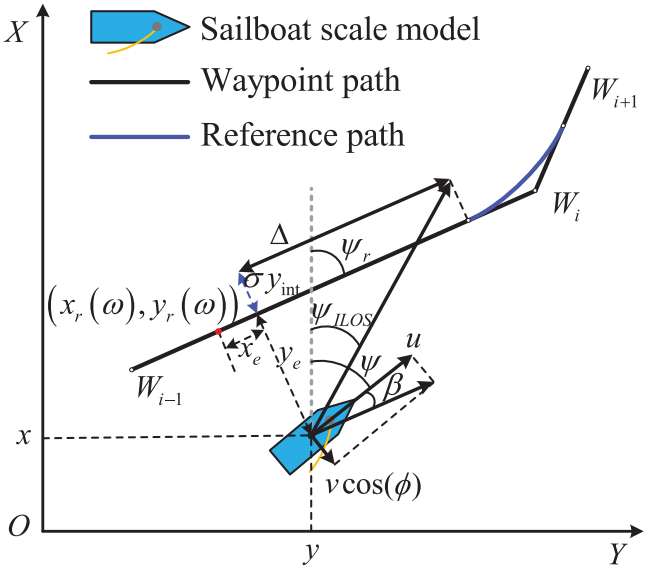

Figure 3. The framework of integral LOS guidance.

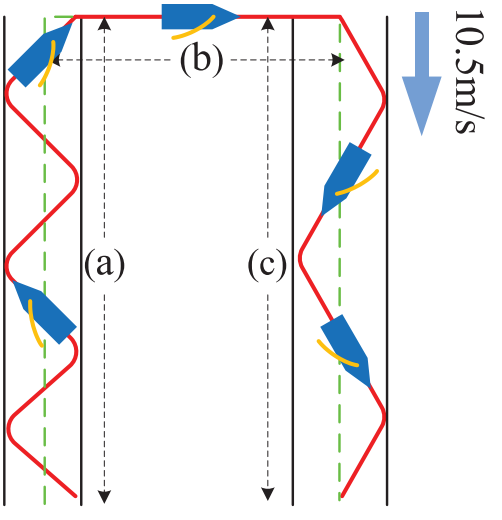

Figure 4. Three sailing modes.

$$\dot{y}_{\text{int}} = \frac{\Delta y_e}{(y_e + y_{\text{int}})^2 + \Delta^2} \tag{15}$$

where Δ and σ are the look-ahead distance and the integral gain, respectively. Both are constant design parameters.

Additionally, to consider the comprehensive cases, that is, navigable, upwind or downwind navigation, see Figure 4.

https://doi.org/10.1017/S0373463319000353 Published online by Cambridge University Press

Navigable mode: Here, the navigable mode is defined by the heading angle being located outside of No-go zones or Do not-go zones, see Figure 2. In this mode, the robot sailboat will sail along the reference path-based waypoints, see Figure 4(b), and the reference heading angle is expressed as:

$$\psi_d = \psi_{ILOS} \tag{16}$$

Upwind mode: For the upwind mode, the heading angle ψ is located in the No-go zone, see Figure 2. The No-go angle related to ψ_{tw} can be expressed as $|\psi_{tw} - \pi \operatorname{sgn}(\psi_{tw}) - \psi_{ILOS}| < \theta_{\max}$, and $\theta_{\max}$ denotes the boundary of upwind no-go zones which shows in the aforementioned polar diagram. In this mode, the robot sailboat will sail with a zigzag path and achieve turning smoothly with a definite distance constraint, along with the reference path while tacking, see Figure 4(a). Furthermore, a sign function $\zeta(t)$ is defined to represent the tacking manoeuvring. $\zeta(t)$ is described by:

$$\zeta(t) = \operatorname{sgn}(y_e(t) + d_{c1} \operatorname{sgn}(\zeta(t-1))) \tag{17}$$

where d_{c1} is the distance constraint for upwind sailing and t, $t-1$ denote the present time point and the last time point, respectively. From Equation (17), $\zeta(t)$ will change its sign if $|y_e| \geq d_{c1}$. Thus, the reference heading angle can be calculated by:

$$\psi_d = \psi_{tw} - \pi \operatorname{sgn}(\psi_{tw}) - \zeta(t)\theta_{\max} - \beta \tag{18}$$

Downwind mode: For the downwind mode, the heading angle ψ is located in the Do not-go zones, see Figure 2. The Do not-go angle related to ψ_{tw} can be expressed as $|\psi_{tw} - \psi_{ILOS}| < \vartheta_{\max}$, and $\vartheta_{\max}$ denotes the boundary of downwind Do not-go zones which shows in the aforementioned polar diagram. To obtain the optimal velocity and shorten the sailing time of the robot sailboat, a zigzag path with a certain distance constraint along the reference path is necessary by employing gybe manoeuvres, see Figure 4(c). Analogous to the upwind mode, the sign function $\zeta(t)$ is expressed as:

$$\zeta(t) = \operatorname{sgn}(y_e(t) + d_{c2} \operatorname{sgn}(\zeta(t-1))) \tag{19}$$

where d_{c2} is the distance constraint for downwind sailing. Thus, the reference heading angle can be calculated by:

$$\psi_d = \psi_{tw} - \zeta(t)\vartheta_{\max} - \beta \tag{20}$$

For Equation (12), the path particle velocity u_p is a virtual input to stabilise the along-track error x_e. Hence, u_p can be devised as:

$$u_p = U \cos(\psi - \psi_r + \beta) + k_x x_e \tag{21}$$

where k_x is a constant parameter.

https://doi.org/10.1017/S0373463319000353 Published online by Cambridge University Press

From Equations (13) and (21), the update law for the path variable ω is expressed as:

$$\dot{\omega} = \frac{U\cos(\psi - \psi_r + \beta) + k_x x_e}{\sqrt{x_r'^2 + y_r'^2}} \tag{22}$$

Noting:

$$\begin{aligned} &\sin\left(\psi - \psi_{ILOS} - \arctan\left(\frac{y_e + \sigma y_{\text{int}}}{\Delta}\right) - \beta + \beta\right) \\ &= \sin\left(\psi_e - \arctan\left(\frac{y_e + \sigma y_{\text{int}}}{\Delta}\right)\right) \\ &= \frac{\Delta}{\sqrt{(y_e + \sigma y_{\text{int}})^2 + \Delta^2}}\sin(\psi_e) - \frac{\Delta}{\sqrt{(y_e + \sigma y_{\text{int}})^2 + \Delta^2}}\cos(\psi_e) \end{aligned} \tag{23}$$

where $\psi_e = \psi - \psi_{ILOS}$.

Substituting Equations (21) and (14) into Equation (12), Equation (24) can be derived:

$$\begin{cases} \dot{x}_e = -k_x x_e + \dot{\psi}_r y_e \\ \dot{y}_e = \dfrac{U\Delta}{\sqrt{(y_e + \sigma y_{\text{int}})^2 + \Delta^2}}\sin(\psi_e) - \dfrac{U y_e}{\sqrt{(y_e + \sigma y_{\text{int}})^2 + \Delta^2}}\cos(\psi_e) - \dot{\psi}_r x_e \end{cases} \tag{24}$$

4. DESIGN OF ROBUST ADAPTIVE NEURAL DAMPING CONTROLLER. In this paper, the control objective is to design a controller that stabilises the heading ψ of the sailboat to the reference heading ψ_d, generated by the improved integral LOS. In this section, the heading and yaw sub-dynamics of system Equations (1) and (2) are chosen. Then an adaptive neural control law is designed by fusing the RBF-NNs and the robust neural damping technique. From the Equations (1) and (2), the following heading and yaw sub-dynamics can be obtained:

$$\begin{cases} \dot{\psi} = r\cos(\phi) \\ \dot{r} = \dfrac{m_u - m_v}{m_r}uv - \dfrac{f_r(\cdot)}{m_r} + \dfrac{g_r(\cdot)}{m_r}u_\delta(\cdot) + d_{wr} \end{cases} \tag{25}$$

with:

$$g_r(\cdot) = -\frac{1}{2}\rho_w A_r U_{ar}^2 |x_r| \tag{26}$$

$$u_\delta(\cdot) = C_{R_L}(\alpha_R) \tag{27}$$

Nevertheless, the precise functional structure of $C_{R_L}(\alpha_R)$ in Equation (6) is unknown. Since the true velocity and bearing angle of current to the rudder is negligible, one can simplify that the apparent velocity of current equates to the sailboat's velocity and the attack angle satisfies $\alpha_R = -\delta_r$, where δ_r is the rudder angle. In Xiao and Jouffroy (2014), a sinusoidal $u_\delta(\cdot)$ was introduced to replace $C_{R_L}(\alpha_R)$ according to table look-up, which can be described as Equation (28):

$$u_\delta(\cdot) = a_1 \sin(-a_2\delta_r) \tag{28}$$

where a_1 and a_2 are the parameters.

https://doi.org/10.1017/S0373463319000353 Published online by Cambridge University Press

Remark 2: The nonlinear mathematical model Equation (25) has been employed in Wille et al. (2016), which is only for the control design. In practical marine engineering, the sailboat is an underactuated vessel because there are only two independent control inputs: sail angle and rudder angle. The thrust in surge is provided primarily by the sail. The rudder mainly affects the yaw motion. The other forces and moments generated by sail, keel and hull can be seen as the model uncertainties $f_r(\cdot)$. Thus, the system model is reasonable and is the basis of the following design.

4.1. *Control design.*

Step 1. The error variable of heading and its derivative are defined as:

$$\psi_e = \psi - \psi_d \tag{29}$$

$$\dot{\psi}_e = r\cos(\phi) - \dot{\psi}_d \tag{30}$$

To stabilise the kinematic error variable Equation (29), a virtual controller α_r is chosen as:

$$\alpha_r = \frac{1}{\cos(\phi)}(-k_\psi \psi_e + \dot{\psi}_d) \tag{31}$$

where k_ψ is the positive design constant.

To avoid repeatedly differentiating the virtual control α_r in the next step, which leads to the so-called "explosion of complexity", the DSC technique (Li, et al., 2010; Xu, et al., 2014) is employed here. A first-order filter β_r is introduced with time constant τ_r. Let α_r pass through it, such that:

$$\tau_r \dot{\beta}_r + \beta_r = \alpha_r, \quad \beta_r(0) = \alpha_r(0) \tag{32}$$

By defining the output error of this filter as $y_r = \beta_r - \alpha_r$, it yields $\dot{\beta}_r = -y_r/\tau_r$ and:

$$\begin{aligned} \dot{y}_r &= \dot{\beta}_r - \dot{\alpha}_r \\ &= -\frac{y_r}{\tau_r} + B_r(\phi, \psi_e, \dot{\phi}, \dot{\psi}_e, \dot{\psi}_d, \ddot{\psi}_d) \end{aligned} \tag{33}$$

where $B_r(\cdot)$ is a bounded continuous function and has a maximum value M_r (please refer to Zhang and Zhang (2015) for details).

Step 2. The error variable r_e and its derivative are defined as:

$$r_e = \alpha_r - r \tag{34}$$

$$\dot{r}_e = \frac{1}{m_r}[m_r\dot{\beta}_r - (m_u - m_v)uv + f_r(\cdot) - g_r(\cdot)u_\delta(\cdot) - m_r d_{wr}] \tag{35}$$

In Equation (35), the unknown function $f_r(\cdot)$ is approximated by RBF-NNs as Equation (36):

$$\begin{aligned} f_r(r) &= \boldsymbol{S}(r)\boldsymbol{A}r + \varepsilon(r) \\ &= \boldsymbol{S}(r)\boldsymbol{A}\beta_r - \boldsymbol{S}(r)\boldsymbol{A}r_e + \varepsilon(r) \\ &= \boldsymbol{S}(r)\boldsymbol{A}\beta_r - -b_r\boldsymbol{S}(r)w_r + \varepsilon(r) \end{aligned} \tag{36}$$

where $\varepsilon(r)$ is the approximation error. Define $b_r = \|\boldsymbol{A}\|_F$, the normalised term $\boldsymbol{A}_r^m = \boldsymbol{A}_r/\|\boldsymbol{A}\|_F$, and thus $w_r = \boldsymbol{A}_r^m r_e$, $b_r w_r = \boldsymbol{A}_r r_e$. Then, the robust neural damping term can be

https://doi.org/10.1017/S0373463319000353 Published online by Cambridge University Press

constructed as Equation (37):

$$v_r \leq \theta_r \varphi_r \tag{37}$$

In Equation (37), $\theta_r = \max\{\|\boldsymbol{A}\|_F, d_r, \bar{\varepsilon} + m_r \bar{d}_{wr}\}$ is the unknown bounded parameter and $\varphi_r = 1 + \xi_r(r) + \|\boldsymbol{S}(r)\| \, \|\beta_r\|$ is the damping term. In addition, $d_r > 0$ is the unknown constant and $\xi_r = u^2/4 + v^2$.

Based on the aforementioned analysis, the error dynamic system Equation (35) can be reformatted as:

$$\dot{r}_e = \frac{1}{m_r}[m_r \dot{\beta}_r + v_r - b_r \boldsymbol{S}(r) w_r - g_r(\cdot) u_\delta(\cdot)] \tag{38}$$

In the adaptive control design, the $\hat{\lambda}_{g_r}$ is the estimation of $\lambda_{g_r} = 1/g_r(\cdot)$, and $\tilde{\lambda}_{g_r} = \lambda_{g_r} - \hat{\lambda}_{g_r}$. The real control for δ_r is designed in Equation (40), where α_u is the desired intermediate control for $g_r(\cdot)u_\delta$. Thus, one can get Equation (39). Considering Equations (28) and (39), the structure function of rudder angle δ_r can be expressed as Equation (42). Furthermore, the matching adaptive law which is updated online to compensate the nonlinear gain uncertainty $g_r(\cdot)$ is expressed as Equation (41), and the detailed analysis will be given in the next section.

$$u_\delta = \hat{\lambda}_{g_r} \alpha_u \tag{39}$$

$$\alpha_u = k_{re} r_e + \dot{\beta}_r + k_{rn} \Psi_r(\cdot) r_e - \psi_e \cos(\phi) \tag{40}$$

$$\dot{\hat{\lambda}}_{g_r} = \sigma_{g_r} \left[\alpha_u r_e - \sigma_r (\hat{\lambda}_{g_r} - \hat{\lambda}_{g_r}(0)) \right] \tag{41}$$

$$\delta_r = -\frac{1}{a_2} \arcsin\left(\frac{1}{a_1} u_\delta \right) \tag{42}$$

In Equations (40), (41) and (42), $\Psi_r(\cdot) = (\phi_r^2 + \boldsymbol{S}(r)^{\mathrm{T}} \boldsymbol{S}(r))/4$, k_{re}, k_{rn}, σ_{g_r}, σ_r a_1, a_2 are the positive design parameters.

Remark 3: In the proposed controller, the control design Equation (40) has a concise form and is easy to implement in practical engineering, benefiting from the following points. (1) Although the incorporated RBF NNs are used to tackle the structure uncertainties, no NNs weights require to be updated online due to the superiority of the robust neural damping technique. (2) This paper tackles the gain uncertainty caused by rudder angle via tuning and compensation online by an adaptive parameter, to improve the availability of the proposed controller in practical marine engineering.

4.2. *Stability Analysis.*

Theorem 1: Consider the closed-loop system composed of subsystems Equations (11) and (25) satisfying the Assumptions 1–3, the error variable Equations (29), (34), the virtual controller Equation (31), the adaptive neural controller Equation (40), and the gain-related adaptive law Equation (41). All initial conditions are satisfied within a compact set $\Omega = \{(x_e, y_e, \psi_e, y_r, \tilde{\lambda}_{g_r}) | x_e^2 + y_e^2 + \psi_r^2 + y_r^2 + r_e^2 + \tilde{\lambda}_{g_r}^2 \leq 2\ell\}$ with any $\ell > 0$, there exists appropriate control parameters $k_x, \tau_r, k_\psi, k_{re}, k_{rn}, \sigma_{g_r}, \sigma_r$ such that all the signals in the closed-loop control system have Semi-Global Uniform Ultimate Bounded (SGUUB)

https://doi.org/10.1017/S0373463319000353 Published online by Cambridge University Press

stability. Furthermore, the output error $\psi_e = \psi - \psi_d$ satisfies $\lim_{t\to\infty} |\psi_e(t)| = \epsilon$ with any $\epsilon > 0$ through tuning the controller parameters.

Proof. According to the control design process, the Lyapunov function candidate is chosen as follows:

$$V = \frac{1}{2}x_e^2 + \frac{1}{2}y_e^2 + \frac{1}{2}\psi_e^2 + \frac{1}{2}y_r^2 + \frac{1}{2}m_r r_e^2 + \frac{1}{2}\frac{g_r(.)}{\sigma_{g_r}}\tilde{\lambda}_{g_r}^2 \tag{43}$$

The time derivative $\dot{V}$ can be derived from Equations (24), (30), (33) and (35):

$$\begin{aligned}
\dot{V} &= x_e\dot{x}_e + y_e\dot{y}_e + \psi_e\,\dot{\psi}_e + y_r\dot{y}_r + m_r r_e\dot{r}_e + \frac{g_r(.)}{\sigma_{g_r}}\tilde{\lambda}_{g_r}\dot{\tilde{\lambda}}_{g_r} \\
&\le -k_x x_e^2 + \frac{U\Delta y_e}{\sqrt{(y_e+\sigma y_{\text{int}})^2+\Delta^2)}}\sin(\psi_e) - \frac{U_{y_e^2}}{\sqrt{(y_e+\sigma y_{\text{int}})^2+\Delta^2}}\cos(\psi_e) \\
&\quad - r_e\psi_e\cos(\phi) - k_\psi\psi_e^2 + y_r\dot{y}_r + r_e\left(m_r\dot{\beta}_r + k_{rn}\Psi_r(.)r_e^2 + \frac{\theta_r^2}{k_{rn}} + \frac{b_r^2 r_e^2}{k_{rn}}\right. \\
&\quad \left. - g_r(.)\lambda_{gr}\alpha_u - g_r(.)\tilde{\lambda}_{g_r}\alpha_u\right) + g_r(.)\tilde{\lambda}_{g_r}\left(\alpha_u r_e - \sigma_r\left(\hat{\lambda}_{g_r} - \hat{\lambda}_{g_r}(0)\right)\right)
\end{aligned} \tag{44}$$

Note that, the following Equations (45), (46), (47) and (48) can facilitate the further derivation using Young's inequality.

$$\begin{aligned}
v_r r_e - b_r \boldsymbol{S}(r) w_r r_e &\le \frac{k_m}{4}\varphi_r^2 r_e^2 + \frac{\theta_r^2}{k_{rn}} + \frac{k_{rn}}{4}\boldsymbol{S}(r)^{\mathrm{T}}\boldsymbol{S}(r)r_e^2 + \frac{b_r^2 w_r^{\mathrm{T}} w_r}{k_{rm}} \\
&= k_{rn}\Psi_r(.)r_e^2 + \frac{\theta_r^2}{k_{rn}} + \frac{b_r^2 w_r^{\mathrm{T}} w_r}{k_{rn}}
\end{aligned} \tag{45}$$

$$\begin{aligned}
w_r^{\mathrm{T}} w_r &= \| \boldsymbol{A}_r^m r_e \|^2 \\
&= \frac{w_{r,1}^{\mathrm{T}} w_{r,1} + w_{r,2}^{\mathrm{T}} w_{r,2} + \cdots + w_{r,n}^{\mathrm{T}} w_{r,n}}{\| \boldsymbol{A}_r \|_{F^2}} r_e^{\mathrm{T}} r_e = r_e^2
\end{aligned} \tag{46}$$

$$\begin{aligned}
m_r\dot{\beta}_r r_e - \dot{\beta}_r r_e &\le (m_r+1)\left|\frac{y_r}{\tau_r}r_e\right| \\
&\le \frac{m_r+1}{\tau_r}r_e^2 + \frac{(m_r+1)}{4}y_r^2
\end{aligned} \tag{47}$$

$$\begin{aligned}
y_r\dot{y}_r &= -\frac{y_r^2}{\tau_r} - y_r\dot{\alpha}_r \\
&= -\frac{y_r^2}{\tau_r} + y_r B_r(\phi, \psi_e, \dot{\phi}, \dot{\psi}_e, \dot{\psi}_d, \ddot{\psi}_d) \\
&\le -\frac{y_r^2}{\tau_r} + \frac{y_r^2 B_r^2 M_r^2}{4aM_r^2} + a \\
&\le -\left(\frac{1}{\tau_r} - \frac{M_r^2}{4a}\right)y_r^2 + a
\end{aligned} \tag{48}$$

Furthermore, inserting the actual control law Equations (40) and (41) into Equation (44), the time derivative $\dot{V}$ is formulated as Equation (49) by utilising the aforementioned

https://doi.org/10.1017/S0373463319000353 Published online by Cambridge University Press

inequations:

$$\dot{V} \le -k_x x_e^2 - \frac{U_{\max}}{\Delta} y_e^2 - k_\psi \psi_e^2 - \left(k_{re} - \frac{m_r+1}{\tau_r} - \frac{b_r}{k_{rn}}\right) r_e^2 - \left(-\frac{m_r+1}{4} + \frac{1}{\tau_r} - \frac{M_r^2}{4a}\right) y_r^2 - \sigma_r \sigma_{gr} \frac{g_r(.)}{\sigma_{g_r}} \tilde{\lambda}_{g_r}^2 + \frac{\theta_r^2}{k_m} - \sigma_r g_r(.) \tilde{\lambda}_{gr} \left(\lambda_{gr} - \hat{\lambda}_{gr}(0)\right) + a + U_{\max} y_e \tag{49}$$

With $U_{\max} = \min\left\{U\Delta / \sqrt{(y_e + \sigma y_{\text{int}})^2 + \Delta^2}\right\}$, then, Equation (49) can be rewritten as:

$$\dot{V} \le -2\kappa V + \varrho \tag{50}$$

where:

$$\kappa = \min\left\{k_x, \frac{U_{\max}}{\Delta}, k_\psi, \left(k_{re} - \frac{m_r+1}{\tau_r} - \frac{b_r}{k_{rn}}\right), \left(-\frac{m_r+1}{4} + \frac{1}{\tau_r} - \frac{M_r^2}{4a}\right), \sigma_r g_r(.)\right\} \tag{51}$$

$$\varrho = \frac{\theta_r^2}{k_{rn}} - \sigma_r g_r(.) \tilde{\lambda}_{g_r} \left(\lambda_{g_r} - \hat{\lambda}_{g_r}(0)\right) + a - U_{\max} y_e \tag{52}$$

We can integrate Equation (50) and obtain $V(t) \le \varrho/2\kappa + (V(0) - \varrho/2\kappa)\exp(-2\kappa t)$. Based on the closed-loop gain shaping algorithm (Zhang and Zhang, 2014), $V(t)$ is bounded, satisfying $\lim_{t\to\infty} V(t) = \varrho/2\kappa$. Thus, all the error signals in the closed-loop control system and the control law Equation (40) are SGUUB under the proposed control scheme. ■

5. ILLUSTRATIVE EXPERIMENTS. In this section, simulation results are presented to verify the effectiveness and superiority of the proposed control scheme. First, a comparative experiment with the result in Xiao and Jouffroy (2014) is presented in Section 5.1. Then, a path following experiment is illustrated in Section 5.2 to verify the system performance in a marine environment. Figure 5 describes the detailed conceptual signal flow box diagram for the closed-loop system, where the marked numbers denote formulae involved in the corresponding box. Here, a 12 m - long keeled sailboat as used in Xiao and Jouffroy (2014) is chosen as the test vessel and it is equipped with one main sail, one keel and one rudder.

As to the external disturbances, a practical marine environment is considered in the simulation, that is: sea wind and irregular wind-generated waves. They are all simulated by employing a physical-based mathematical model. The Competitive Standing of the Norwegian Offshore Sector (NORSOK) wind and the Joint North Sea Wave Observation Project (JONSWAP) wave spectrums are adapted to produce these disturbances, which have been detailed in Fossen (2011). Figure 6 describes the slow time-varying directional wind field and the waves surface with fifth level sea state, generated by wind. The main speed $U_{tw} = 10{\cdot}5$ m/s, wind direction $\psi_{tw} = 0$ deg.

5.1. *The comparative experiment.* In this section, a comparative experiment is used to demonstrate the effectiveness of the developed adaptive neural controller and its merits in the matter of practical marine environment disturbance, uncertain structure

https://doi.org/10.1017/S0373463319000353 Published online by Cambridge University Press

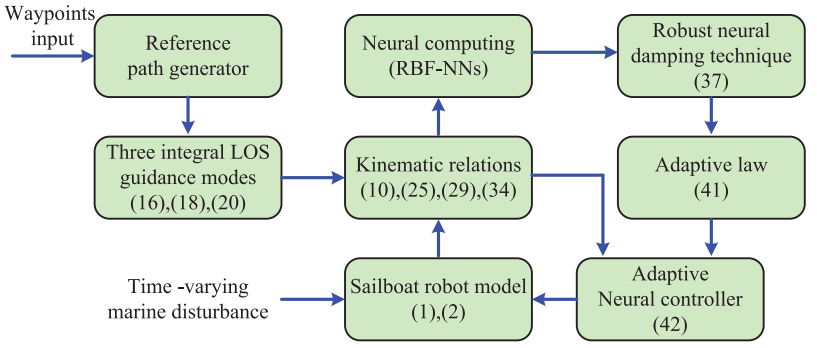

Figure 5. Conceptual signal flow box diagram for path-following control.

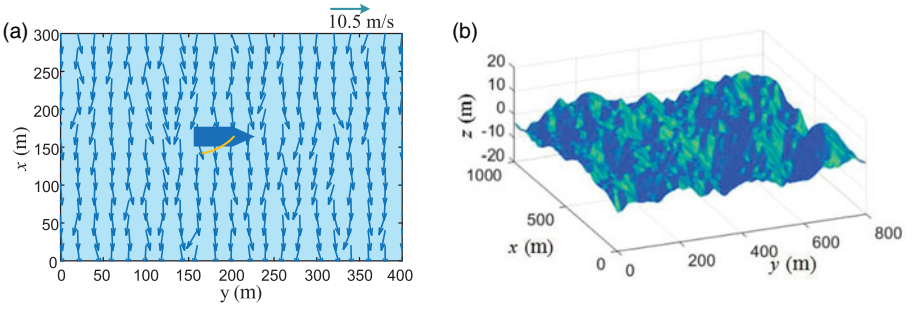

Figure 6. Marine environment disturbance with fifth level sea state $\psi_{tw} = 0$ deg: (a) 2-D sketch field of surface wind. (b) Corresponding wind-generated waves.

and gain-uncertainty in the existing result (Xiao and Jouffroy, 2014). The desired course angle for the sailboat robot is $\psi_d = 60$ deg, and the initial states of the sailboat robot are $[x(0), y(0), \phi(0), \psi(0), u(0), v(0), p(0), r(0), \delta_s(0), \delta(0)] = [-20\,\text{m}, 0\,\text{m}, 0\,\text{deg}, 0\,\text{deg}, 1\,\text{m/s}, 0\,\text{m/s}, 0\,\text{deg/s}, 0\,\text{deg/s}, 0\,\text{deg}, 0\,\text{deg}]$. For the compared control algorithm, the related parameters setting uses the values in Equation (54). The RBF NN in the control algorism is used to approximate the structure uncertainty. It contains 25 nodes, that is, $l = 25$, with centres spaced by $[-2{\cdot}5\,\text{m/s}, 2{\cdot}5\,\text{m/s}] \times [-2{\cdot}5\,\text{m/s}, 2{\cdot}5\,\text{m/s}] \times [-0{\cdot}6\,\text{rad/s}, 0{\cdot}6\,\text{rad/s}]$ for $f_r(\cdot)$, widths $\mu_i = 3$ $(i = 1, 2, \ldots, l)$.

The response curves of the closed-loop systems under the two control algorithms are presented in Figure 7. The second curve describes the response of the rudder angle which considers the rudder servo. It is of note that the two control algorithms have a similar steady performance, but under the proposed control algorithm, the sailboat has a superior convergence speed. For quantitative purposes, three popular performance specifications in Equation (53) are employed to evaluate the corresponding algorithms. These are the Mean Absolute Error (*MAE*), the Mean Absolute control Input (*MAI*) and the Mean Total Variation (MTV) of the control. *MAE* can be used for measuring the performance of the system response and *MAI* and *MTV* are used for measuring properties of energy consumption and smoothness (Zhang and Zhang, 2014). The corresponding quantitative valuation of the comparative experiment is measured and summarised as shown in Table 1. The proposed

https://doi.org/10.1017/S0373463319000353 Published online by Cambridge University Press

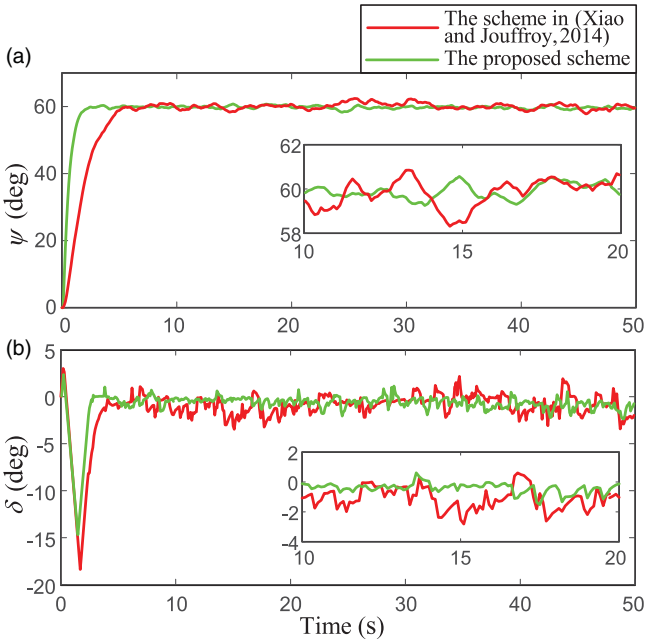

Figure 7. Comparison of control efforts: the proposed scheme (green line) and the control scheme in Xiao and Jouffroy (2014) (red line).

Table 1. Quantitative comparison of performances for the proposed scheme and the one in Xiao and Jouffroy (2014).

Indexes	Items	The proposed controller	The controller in Xiao and Jouffroy (2014)
MAE	ψ_e	1·3935	2·7864
MAI	δ(deg)	1·0648	1·7675
MTV	δ(deg)	0·0868	0·1364

algorithm has improved closed-loop performance and energy efficiency.

$$\begin{aligned} MAE &= \frac{1}{t_{\text{end}} - 0}\int_0^{t_{\text{end}}} |e(t)|\,\mathrm{d}t \\ MAI &= \frac{1}{t_{\text{end}} - 0}\int_0^{t_{\text{end}}} |u(t)|\,\mathrm{d}t \\ MTV &= \frac{1}{t_{\text{end}} - 0}\int_0^{t_{\text{end}}} |u(t+1) - u(t)|\,\mathrm{d}t \end{aligned} \tag{53}$$

5.2. *The path following experiment.* To gather the ocean data, a reference path is planned, which is generated by waypoints $W_1(0,0)$, $W_2(600,0)$, $W_3(900,900)$, $W_4(600,180)$, $W_5(0,1800)$, $W_6(0,500)$ with units m. The initial states of the URS are $[x(0), y(0), \phi(0), \psi(0), u(0), v(0), p(0), r(0), \delta_s(0), \delta(0)]$ = [−20 m, 0 m, 0 deg, 0 deg, 1 m/s, 0 m/s, 0 deg/s, 0 deg/s, 0 deg, 0 deg]. For the proposed control algorithm, the parameters are set

https://doi.org/10.1017/S0373463319000353 Published online by Cambridge University Press

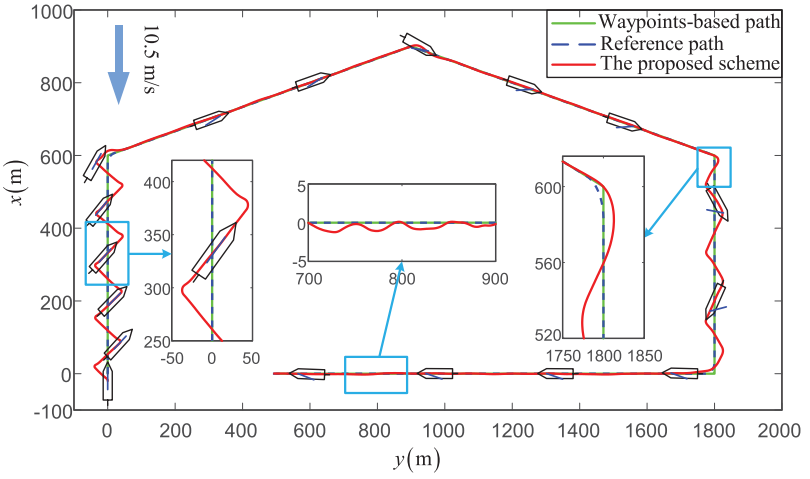

Figure 8. The path-following trajectory of the sailboat under the proposed scheme.

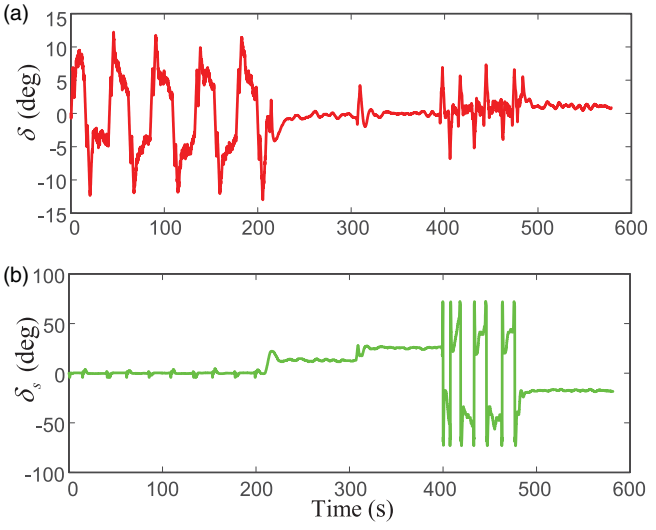

Figure 9. Control inputs under the proposed scheme.

as shown in Equation (54).

$$\begin{aligned} &\Delta = 20\,\text{m}, \sigma = 0{\cdot}01, \theta_{\max} = \pi/4, \vartheta_{\max} = \pi/6, d_{c1} = 40\,\text{m}, \\ &d_{c2} = 25\,\text{m}, k_x = 0{\cdot}5, k_\psi = 0{\cdot}1, k_{re} = 0{\cdot}5, \sigma_{gr} = 0{\cdot}02, \\ &\sigma_r = 0{\cdot}5, \tau_r = 0{\cdot}1, k_{rn} = 0{\cdot}3, a_1 = 1{\cdot}2, a_2 = 2{\cdot}0 \end{aligned} \tag{54}$$

Figure 8 illustrates the simulated experiment of a path-following trajectory fusing the improved integral LOS guidance and adaptive neural control strategies with the simulated marine environment. The developed path-following control scheme shows an obviously good performance, and it could effectively control the sailboat for the path following mission along with the waypoints. In particular, while the sailboat sails in the upwind and

https://doi.org/10.1017/S0373463319000353 Published online by Cambridge University Press

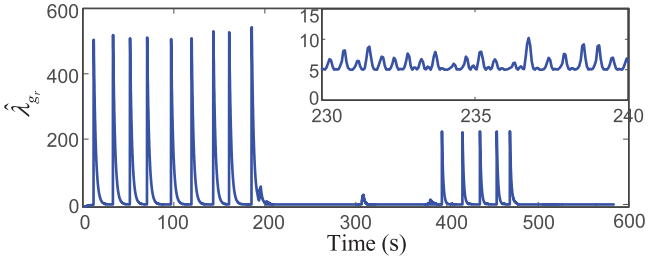

Figure 10. Adaptive adjusting parameter under the proposed scheme.

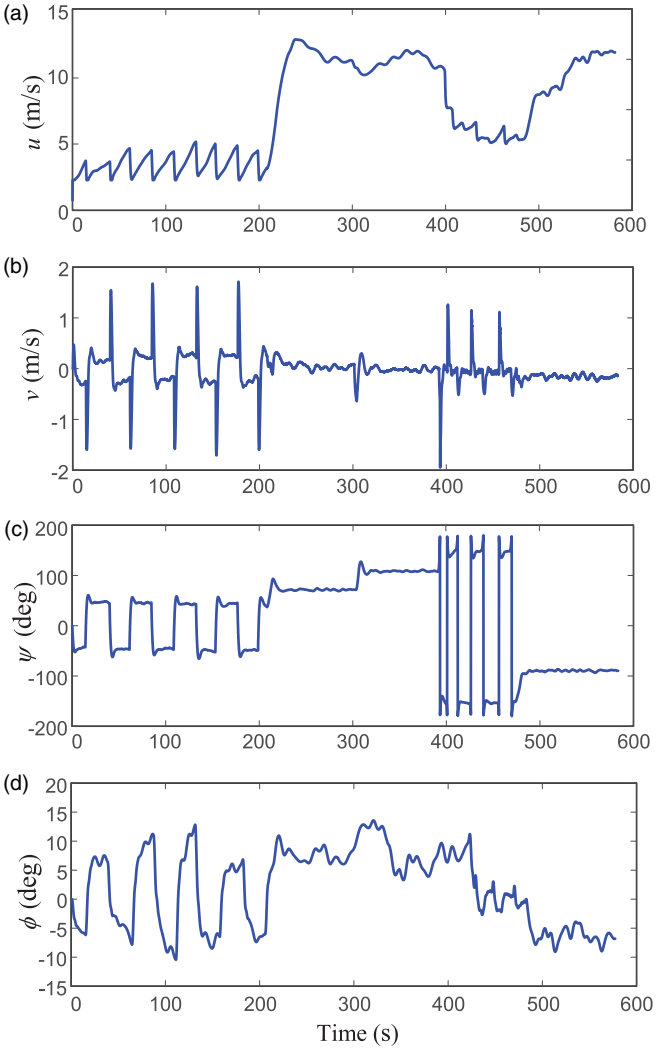

Figure 11. The attitude variables of the sailboat under the proposed scheme.

https://doi.org/10.1017/S0373463319000353 Published online by Cambridge University Press

downwind legs, the improved integral LOS guidance scheme can achieve a zigzag trajectory and automatic turn manoeuvring with safety bandwidth constraints. As is shown in Figure 8, the green solid line denotes the path based-waypoints. The blue dashed line denotes the reference path. The red solid line is the dynamic trajectory of the URS, with the ship shape curve to describe its attitudes.

The control inputs δ_S and δ are presented in Figure 9 with the simulated marine environment. It is obvious that the control inputs are within a reasonable range. Figure 10 describes the estimation of the adaptive parameter which is updated online to stabilise the effect of the gain uncertainty. It can be seen that the adaptive parameter changes drastically at 200 seconds due to the sailboat navigating in the upwind mode, especially when it is tacking. The upwind or downwind leg could increase the complexity and difficulty. Figure 11 presents the attitude variables of the sailboat, u, v, ψ, ϕ under the proposed control scheme. It can be noted that the attitude variables are Uniform Ultimate Bounded (UUB) in the simulated experiment. Therefore, it has been demonstrated that the proposed path-following control scheme has a fine performance in practical marine engineering. Based on the above experiments, the developed improved integral LOS guidance scheme and adaptive neural controller have a strong performance in terms of control performance, self-steering and have a small computation burden. In particular, the scheme with improved integral LOS guidance and the robust neural damping technique is more in accordance with practical marine engineering.

6. CONCLUSION. In this paper, a novel strategy is studied for waypoint-based path following control for a URS in a practical marine environment. An improved integral LOS-based guidance principle is developed to enhance the automatic navigation of a robot sailboat, including the navigable mode, upwind mode and downwind mode. The intelligent heading selection strategy can assure a smooth switchover of modes while sailing in upwind or downwind modes. Furthermore, an adaptive neural controller is developed to control the heading ψ to converge to the objective ψ_d quickly, and the URS sails within a small neighbourhood of the waypoint-based reference path. The SGUUB stability of the closed-loop system is proved via the Lyapunov theory. In contrast from the existing results, the performance of the control scheme is more in accordance with the engineering requirements in its advantages of concise form, robustness and small computational burden. Simulation experiments have been presented under a simulated marine environment and the main results have demonstrated the effectiveness of the proposed control system.

ACKNOWLEDGMENT

This research is partially supported by the National Postdoctoral Program for Innovative Talents (No. BX201600103), the Doctoral Scientific Research Foundation of Liaoning Province (No. 20170520189, 20180520039), the Program for Innovative Research Team in University (No.IRT17R13), the Fundamental Research Funds for the Central Universities (No. 3132018301, 3132018304, 3132016315), the National Natural Science Foundation of China (No. 61473183, 51679024) and the China Postdoctoral Science Foundation (No. 2016M601600). The authors would like to thank the anonymous reviewers for their valuable comments to improve the quality of this article.

REFERENCES

Abril, J., Salom, J. and Calvo, O. (1997). Fuzzy control of a sailboat. *International Journal of Approximate Reasoning*, **16**(4), 359–375.

Alves, J. C. and Cruz, N. A. (2014). A mission programming system for an autonomous sailboat. *Oceans Conference.* St Johns, CANADA.

Arredondo-Galeana, A. and Viola, I. M. (2018). The leading-edge vortex of yacht sails. *Ocean Engineering*, **159**, 552–562.

Caharija, W., Pettersen, K. Y., Gravdahl, J. T. and Borhaug, E. (2012). Integral LOS guidance for horizontal path following of underactauted autonomous underwater vehicles in the presence of vertical ocean currents. *2012 American Control Conference.* Montreal, Canada.

Carter, W. E. and Carter, M. S. (2010). The age of sail: A time when the fortunes of nations and lives of seamen literally turned with the winds their ships encountered at sea. *The Journal of Navigation*, **63**, 717–731.

Corno, M., Formentin, S. and Savaresi, S. M. (2016). Data-driven online speed optimization in autonomous sailboats. *IEEE Transactions on Intelligent Transportation Systems*, **17**(3), 762–771.

Deng, Y., Zhang, X. and Zhang, G. (2018). Fuzzy logic based speed optimization and path following control for sailassisted ships. *Ocean Engineering*, **171**, 300–310.

Do, K. D. (2010). Practical control of underactuated ships. *Ocean Engineering*, **37**, 1111–1119.

Fossen, T. I. (2011). *Handbook of Marine Craft Hydrodynamics and MotionControl*. New York, Wiley.

Guo, Y., Romero, M., Ieng, S.-H., Plumet, P., Benosman, R. and Gas, B. (2011). Reactive path planning for autonomous sailboat using an omni-directional camera for obstacle detection. *Proceedings of the 2011 IEEE International Conference on Mechatronics.* Istanbul, Turkey.

Illingworth, J. H. (1997). Navigation and strategy in ocean racing. *The Journal of Navigation*, **50**(3), 381–389.

Li, T.-S., Wang, D., Feng, G. and Tong, S.-C. (2010). A DSC approach to robust adaptive NN tracking control for strict-feedback nonlinear systems. *IEEE Transactions on Systems, Man, and Cybernetics*, **40**(3), 15–27.

Li, Y. and Tong, S. (2018a). Adaptive neural networks prescribed performance control design for switched interconnected uncertain nonlinear systems. *IEEE Transactions on Neural Networks and Learning Systems*, **29**(7), 3059–3068.

Li, Y. and Tong, S. (2018b). Fuzzy adaptive control design strategy of nonlinear switched large-scale systems. *IEEE Transactions on Systems, Man and Cybernetics: Systems*, **48**(12), 2209–2218.

Perez, T. (2005). *Ship Motion Control (Course keeping and roll stabilisation using rudder and fins)*. London, Springer.

Petres, C., Romero-Ramirez, M.-A. and Plumet, F. (2012). A potential field approach for reactive navigation of autonomous sailboats. *Robotics and Autonomous Systems*, **6**(5), 1520–1527.

Plumet, F., Petres, C., Romero-Ramirez, M.-A., Gas, B. and Ieng, S.-H. (2015). Toward an autonomous sailing boat. *IEEE Journal of Oceanic Engineering*, **40**(2), 397–407.

Qiao, L. and Zhang, W. (2018). Double-Loop Integral Terminal Sliding Mode Tracking Control for UUVs With Adaptive Dynamic Compensation of Uncertainties and Disturbances. *IEEE Journal of Oceanic Engineering*, **2**, 1–25.

Serrano, M. E., Scaglia, G. J. E., Godoy, S. A., Mut, V. and Ortiz, O. A. (2014). Trajectory tracking of underactuated surface vessels: A linear algebra approach. *IEEE Transactions on Control System Technology*, **22**(3), 1103–1111.

Statheros, T., Howells, G. and Maier, K. M. (2008). Autonomous ship collision avoidance navigation concepts, technologies and techniques. *The Journal of Navigation*, **61**(1), 129–142.

Stelzer, R. and Proll, T. (2008). Autonomous sailboat navigation for short course racing. *Robotics and Autonomous Systems*, **56**(7), 604–614.

Tagliaferri, F. and Viola, I. M. (2017). A real-time strategy-decision program for sailing yacht races. *Ocean Engineering*, **134**, 129–139.

Tagliaferri, F., Philpott, A. B., Viola, I. M. and Flay, R. G. J. (2014). On risk attitude and optimal yacht racing tactics. *Ocean Engineering*, **90**(4), 149–254.

Viel, C., Vautier, U., Wan, J. and Jaulin, L. (2018). Position keeping control of an autonomous sailboat. *11th IFAC Conference on Control Applications in Marine Systems, Robotics, and Vehicles (CAMS).* Opatijia, Croatia.

Wille, K. L., Hassani, V. and Sprenger, F. (2016). Modeling and course control of sailboats. *IFAC PapersOnLine*, **49**(23), 532–539.

Xiao, K., Sliwka, J. and Jaulin, L. (2011). A wind-independent control strategy for autonomous sailboats based on voronoi diagram. *CLAWAR 2011.* France.

Xiao, L. and Jouffroy, J. (2014). Modeling and nonlinear heading control of sailing yachts. *IEEE Journal of Oceanic Engineering*, **39**(2), 256–268.

Xu, B. and Shou, Y. (2018). Composite Learning Control of MIMO Systems with Applications. *IEEE Transactions on Industrial Electronics*, **65**(8), 6414–6424.

Xu, B. and Sun, F. (2018). Composite Intelligent Learning Control of Strict-Feedback Systems with Disturbance. *IEEE Transactions on Cybernetics*, **48**(2), 730–741.

Xu, B., Shi, Z., Yang, C. and Sun, F. (2014). Composite Neural Dynamic Surface Control of a Class of Uncertain Nonlinear Systems in Strict-Feedback Form. *IEEE Transactions on Cybernetics*, **44**(12), 2626–2634.

Yeh, E. C. and Bin, J.-C. (1992). Fuzzy control for self-steering of a sailboat. *International Conference on Intelligent Control and Instrumentation.* Singapore.

Zhang, G. and Zhang, X. (2014). Concise robust adaptive path-following control of under-actuated ships using DSC and MLP. *IEEE Journal Ocean Engineering*, **39**(4), 685–694.

Zhang, G. and Zhang, X. (2015). A novel DVS guidance principle and robust adaptive path following control for underactuated ships using low frequency gain-learning. *ISA Transactions*, **56**, 75–85.

Zhang, G., Deng, Y. and Zhang, W. (2017). Robust neural path-following control for underactuated ships with the DVS obstacles avoidance guidance. *Ocean Engineering*, **143**, 198–208.

Zhang, G., Zhang, X. and Zhang, Y. (2015). Adaptive neural path-following control for underactuated ships in fields of marine practice. *Ocean Engineering*, **104**(8), 558–567.